Physics in Medicine &
Biology

PAPER • **OPEN ACCESS**

Direct measurement of relative stopping power maps of prosthesis devices and synthetic materials by proton computed tomography

To cite this article: Mara Bruzzi *et al* 2026 *Phys. Med. Biol.* **71** 015041

View the article online for updates and enhancements.

You may also like

- Three dimensional segmentation of abdominal arteries and veins using vision transformers and domain adaptation
Panpan Wu, Yurou Xu, Ziping Zhao et al.
- Intercomparisons of computed epithelial/absorbed power density and temperature rise in anatomical human face models under localized exposures at 10 GHz and 30 GHz
Kun Li, Sachiko Kodera, Dragan Poljak et al.
- Anti-scatter grid performance in digital mammography and contrast-enhanced mammography: a Monte Carlo study
Franziska Mauter, Mathias Anton, Ruben van Engen et al.

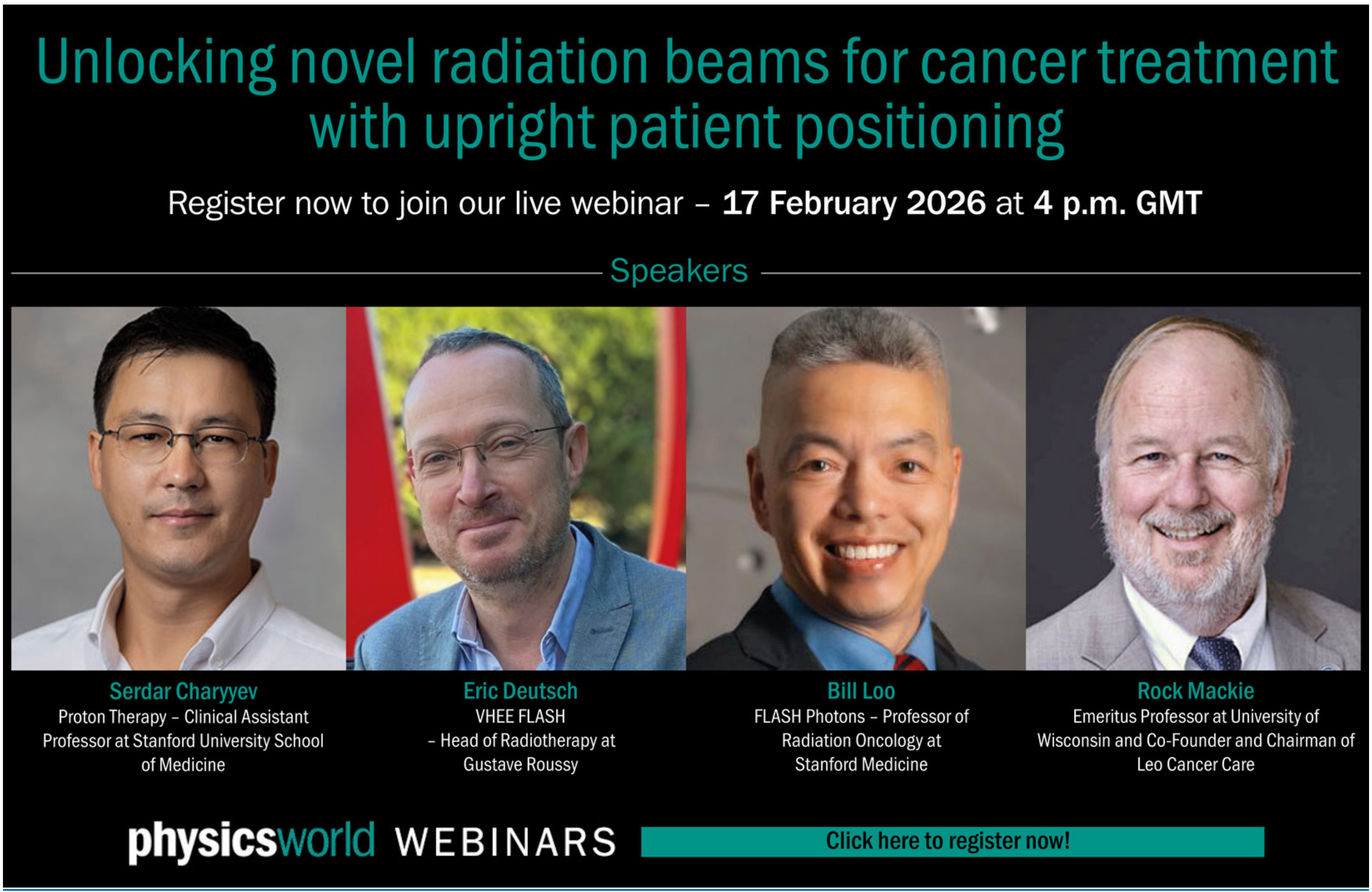

Unlocking novel radiation beams for cancer treatment with upright patient positioning

Register now to join our live webinar – **17 February 2026** at **4 p.m. GMT**

Speakers

Serdar Charyyev
Proton Therapy – Clinical Assistant Professor at Stanford University School of Medicine

Eric Deutsch
VHEE FLASH – Head of Radiotherapy at Gustave Roussy

Bill Loo
FLASH Photons – Professor of Radiation Oncology at Stanford Medicine

Rock Mackie
Emeritus Professor at University of Wisconsin and Co-Founder and Chairman of Leo Cancer Care

physicsworld WEBINARS

Click here to register now!

This content was downloaded from IP address 77.83.113.77 on 03/02/2026 at 09:55

IOP Publishing
Phys. Med. Biol. 71 (2026) 015041
https://doi.org/10.1088/1361-6560/ae2c38

Physics in Medicine & Biology

IPEM
Institute of Physics and Engineering in Medicine

OPEN ACCESS

RECEIVED
18 June 2025

REVISED
3 November 2025

ACCEPTED FOR PUBLICATION
12 December 2025

PUBLISHED
14 January 2026

PAPER

Direct measurement of relative stopping power maps of prosthesis devices and synthetic materials by proton computed tomography

Mara Bruzzi[1,2,*], **Monica Scaringella**[2], **Roberto Righetto**[3,4], **Elena Fogazzi**[3,5], **Francesco Fracchiolla**[3,4], **Francesco Tommasino**[3,5], **Enrico Verroi**[3], **Stefano Lorentini**[3,4] **and Carlo Civinini**[2]

[1] Department of Physics and Astronomy University of Florence, Via G. Sansone 1, Sesto Fiorentino, FI, Italy
[2] Istituto Nazionale di Fisica Nucleare INFN Firenze, Via G. Sansone 1, Sesto Fiorentino, FI, Italy
[3] Istituto Nazionale di Fisica Nucleare TIFPA, Via Sommarive 14, Povo, TN, Italy
[4] Medical Physics Unit, Hospital of Trento, Azienda Provinciale Servizi Sanitari (APSS), Trento, Italy
[5] Department of Physics University of Trento, Via Sommarive 14, Trento, TN, Italy
[*] Author to whom any correspondence should be addressed.

E-mail: mara.bruzzi@unifi.it

Keywords: proton tomography, stopping power measurements, prosthesis, proton therapy

Abstract

Objective. Treatment planning in proton therapy requires an accurate estimation of stopping power ratio relative to water (SPR) maps. Presently, about 4% of patients submitted to radiotherapy treatments have metallic implants, which are responsible for an incorrect determination of SPRs in prostheses and surrounding regions. This study presents the first application of the proton computed tomography (pCT) technique, able to directly measure SPRs maps, on complex metallic implants. *Approach.* A homogeneous Ti6Al4V alloy sample, a set of metallic devices used for prostheses and an intra-vertebral titanium alloy implant have been inspected, by means of a prototype pCT system with a 5×20 cm^2 field-of-view (FoV) developed by INFN Firenze (Italy), under a proton beam at Trento Proton Therapy Centre (APSS, Trento, Italy). For comparison, a Multi Layer Ionization Chamber (MLIC) has been used to independently determine the SPR mean value of the Ti6Al4V alloy sample. *Main Results.* Tomographic reconstructions of all devices and materials have been performed and SPR maps have been obtained. All pCT images and profiles, even of metallic components, are characterized by negligible artifacts. The fine spatial resolution of our pCT system, about 0.7 lp mm^{-1}, allowed us to resolve details within a millimeter scale. The internal grid of the meshed cage as well as details of the screws' head of the intra-vertebral titanium alloy implant are clearly visible. The SPR of the Ti6Al4V alloy sample measured with pCT, 3.14 ± 0.02, compares well with what was measured by MLIC: 3.17 ± 0.02. *Significance.* This study presents the first application of the pCT methodology to directly measure SPR maps of complex metal prostheses. The ability of pCT to correctly determine mean SPR values has been experimentally demonstrated. Furthermore, this technique was shown to reconstruct complex metal structures at the millimeter scale with negligible artifacts.

1. Introduction

Hounsfield units (HU) distributions, obtained from x-ray computed tomography (xCT) imaging, are used as the primary source of electron density representation of tissues. After conversion to stopping power ratio relative to water (SPR), they currently form the basis for range and dose calculations in proton beam radiotherapy (Schneider *et al* 1996, Knopf and Lomax 2013). Nonetheless, xCT image quality may be affected by artifacts leading to unwanted inaccuracies in the treatment planning (TP) (Jakel and Reiss 2007). One of the most important sources of artifacts are metallic prostheses, usually made of materials composed of high atomic number elements (Rousselle *et al* 2020).

Presently, about 4% of patients submitted to radiotherapy treatments have metallic implants and this number is constantly growing (Le Fèvre *et al* 2022). Implants utilize a wide range of metallic alloys and composites. Especially, Titanium and Ti alloys as Ti6Al4V play a dominant role among medical implants. In load-bearing orthopedic implants they are especially useful because of their high mechanical strength and resistance to corrosion; they are also used in the manufacturing of bone plates, screws, and other fixation devices. Ti alloys are used in spinal fusion surgeries for cages, rods, and screws in the spinal column, to treat various spinal disorders. Moreover, Ti's non-reactive nature makes it suitable for use in heart valves and pacemakers, and in general in casings of cardiovascular implants. In reconstructive surgery, particularly for facial bones, Ti plates and screws are used to stabilize the bone structure (Abd-Elaziem *et al* 2024).

High density of metallic implants may be not correctly converted to HUs due to the limited acquisition windows of standard xCT scans and to photon starvation. HUs assigned to metallic implants may saturate producing identical values regardless of implant composition. Recently developed carbon fiber reinforced and Polyetheretherketone implants partially overcome this issue (Cofano *et al* 2020, Long Maziyar *et al* 2023). Carbon screws may be coated by titanium for improved osteo-integration (Poel *et al* 2020).

Since the proton range is directly dependent on the electron density of the material being traversed, imaging problems associated with prostheses may be responsible for uncertainties in the particle range in irradiated tissues. Furthermore, due to the high doses delivered in the Bragg peak at the end of the particles' trajectory, any range uncertainty in proton therapy can translate into a significant difference between the delivered and the planned dose. For example, when measuring the dose in the proximity of metallic screws commonly implanted in patients with spinal diseases, an overestimation of 12% and 8% was reported for stainless steel and Ti screws, respectively (Jia *et al* 2015). Furthermore, the effect of secondary particles in patients with and without metallic hip implants was investigated and an increase by a factor 9 and 6 of the absorbed dose behind Ti and stainless-steel hip prostheses, respectively, was reported when implants were close to the Bragg peak (Oancea *et al* 2018). High-dose proton therapy in the adjuvant treatment of spinal chordomas in the presence of metallic surgical stabilization was predictive of worse outcomes (Snider *et al* 2018).

As a result, proton radiotherapy in patients carrying metallic prostheses is a complex treatment. Specific guidelines to summarize safe and optimal delivery of proton beam therapy (PBT) are being developed by the scientific community. As an example, a consensus statement for PBT in spinal tumor treatment has been recently reported in Chhabra *et al* (2024), while a study on PBT options for prostate cancer patients with hip prosthesis is reported in (Moteabbed *et al* 2024).

Possible solutions to mitigate these effects are SPR calculation methods with Monte Carlo simulations, to model with higher accuracy the interactions of protons with implants (Mairani *et al* 2013) and the development of Metal Artifact Reduction (MAR) algorithms (Andersson *et al* 2018, Branco *et al* 2021, Njiti *et al* 2024, Selles *et al* 2024).

Furthermore, to overcome the source of inaccuracies, inclusion of material-specific SPR data for commonly used implant materials may be adopted. Nonetheless, this latter methodology suffers the drawback that implants are often complex structures made of many different elemental composites. Therefore, material-specific SPR may be difficult to be known *a-priori*.

An innovative methodology to directly determine material-specific SPRs, even for metals, is proton computed tomography (pCT) (Sadrozinski *et al* 2003, Bashkirov *et al* 2016, Bruzzi *et al* 2017, Civinini *et al* 2020, Johnson 2024). In fact, a first quantitative comparison of artifacts produced by metal prostheses in pCT and x-CT was reported in Civinini *et al* (2020) using an anthropomorphous head phantom carrying a titanium spinal bone prosthesis and a tungsten dental filling. Reconstructed pCT images taken with 211 MeV proton beams evidenced a significant reduction of artifacts in the proximity of prostheses of pCT images against those obtained with xCT. Experimental results reported for stopping power of metals (iron and copper) directly measured with pCT, showed a good agreement with expected NIST values (Bruzzi *et al* 2017), confirming that protons' energy loss in metal is more correctly evaluated by pCT than through x-rays attenuation coefficients in x-CT.

To fully exploit the promising potential of pCT in improving proton therapy treatment accuracy, one can follow two different pathways. First, which may be cumbersome at present state of technology, is to apply pCT directly to patients with prosthesis. A second way, we propose in this paper, is to create a reliable set of SPR effective values for implant materials and devices to be implemented in the TP of the patient. To this purpose, this study presents the first application of pCT to realistic metallic implants of different geometries and elemental compositions, to directly obtain their SPRs. Maps obtained by pCT with a variety of prostheses materials are presented and discussed. A set of metallic devices used as spinal implants (intra-vertebral cages, screws, …) placed inside a water phantom have been imaged

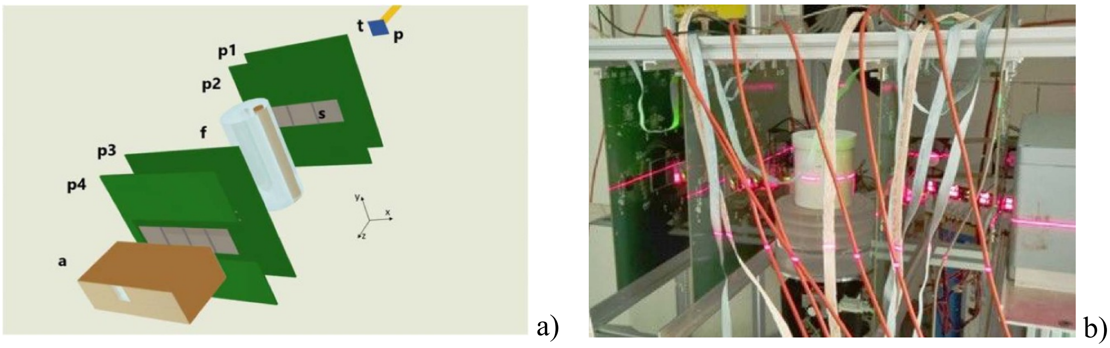

Figure 1. (a) Sketch of the pCT system: a: YAG:Ce calorimeter, *p*1–*p*4: tracker planes, *s*: silicon microstrip sensors, *f*: phantom, *p*: beam pipe; *t*: tantalum scattering plate (distance from tracker not to scale). The overlap sensor regions are visible in darker grey in the silicon microstrip sensors windows. Reproduced from Scaringella *et al* 2023. The Author(s). CC BY 4.0. (b) Photograph of the pCT system at the experimental beam line of Trento Proton Therapy Centre APSS, Trento, Italy.

by pCT under a 211 MeV proton beam at the proton-therapy centre of APSS (Azienda Provinciale per i Servizi Sanitari, Trento, Italy). Tomographic images have been reconstructed and SPR values of implant materials have been determined. Measured values prove the benefit of direct SPR determination through pCT and could open the way to a direct implementation of this methodology in TP procedures in proton therapy.

2. Experimental methods

2.1. pCT system

Figure 1(a) shows a sketch of the pCT system used in this work. The experimental apparatus, characterized by a nominal 5 × 20 cm^2 field of view (FoV), is composed of a tracker and a calorimeter (Scaringella *et al* 2023). The tracker allows to determine the position and direction of each proton before and after the phantom, the calorimeter provides the measurement of the residual energy of each proton exiting the phantom. The tracker consists of four planes, placed two upstream and two downstream the phantom. Each plane is made of a 200 μm-pitch silicon microstrip detectors 4 × 1 sensors grid in view to measure x–y local coordinates of the incident proton (z nominal beam direction). The calorimeter is a segmented YAG:Ce scintillating detector, composed of a 2 × 7 crystals matrix each with a front size of 3 × 3 cm^2 and a length of 10 cm which is enough to fully absorb protons of kinetic energy as large as 230 MeV. The scintillation light emitted by each crystal is converted to a voltage signal by silicon photodiodes directly coupled to crystals backside. The pCT calorimeter is also used to trigger the single-event electronic readout system. A more detailed description of the pCT apparatus can be found in Civinini *et al* (2020), Scaringella *et al* (2023). Previous characterization studies demonstrated a SPR calibration accuracy and reproducibility of the pCT system below 1% (Fogazzi *et al* 2023, Scaringella *et al* 2023). Figure 1(b) shows the pCT apparatus mounted in the experimental room of the APSS-Trento Proton Therapy Centre where a cyclotron (IBA, Proteus 235) is used to produce proton beams with energies in the range 70–228 MeV (Tommasino *et al* 2017).

A 2.5 mm thick tantalum scattering plate is placed immediately downstream the beam pipe exit window to widen the beam, ensuring the proton flux covers the whole FoV of the pCT system (5 × 20 cm^2). Between the second and the third tracker plane, the phantom is placed on a remotely controlled rotating platform. The data-taking for each phantom's image used in this paper, performed at 100 kHz, corresponds to about 1.3–1.4 × 10^9 triggers, for a whole duration of about 3.5 h. The nominal proton energy at the beam pipe exit window for the tomographic data-taking was 211 MeV. The number of projections was 400 with a uniform angular step of 0.9°. The alignment, calibration and event reconstruction procedure were extensively described in Bashkirov *et al* (2016). The algorithm used to reconstruct all the images in this paper is described in Rit *et al* (2013). It is a filtered back projection algorithm based on Feldkamp's reconstruction algorithm (Feldkamp *et al* 1984) considering the 'most likely path' of each proton as it is defined in Williams (2004), Schulte *et al* (2008). All pCT SPRs measured in this work are relative to the NIST PSTAR water value at the density of 1 gcm^{-3} (Berger *et al* 2017) at 4 °C temperature. Almost all the tomographic images shown in this article have been reconstructed using 390 × 390 × 1500 μm^3 voxel sizes. In some cases, when a finer coronal view is needed, the reconstruction voxel size has been reduced to 390 × 390 × 390 μm^3. The SPR values of the materials studied in this paper are calculated from the distributions of the values of individual voxels in given regions of interest (ROIs). The systematic errors on these values are due, on one side, to the calorimeter energy inhomogeneities (±0.5%) (Scaringella *et al* 2023), and on the other side, to the event cuts used on datasets before the reconstruction process (±0.4%). This last contribution is due to the removal of the nuclear interaction events in the calorimeter material which, in some cases, are indistinguishable from the good events. In fact, nuclear interactions in the calorimeter produce secondaries with high LET, which light emission is quenched by the Birks effect. As a consequence, the energy measured for these events is underestimated, so they should be removed from the reconstruction. The ±0.4% uncertainty has been evaluated as the difference in the measurements of the SPR of the water using two independent removal methods. The statistical errors, calculated from the Gaussian best-fit of the experimental SPR distributions, due to the high number of pixels in the ROIs, are far lower than systematic ones and thus are neglected.

For comparison, a multi layer ionization chamber (MLIC) (Giraffe, IBA Dosimetry, Schwarzenbruck, Germany) has been used to independently measure the SPR mean value of a homogeneous cylindrical (3 cm diameter, 1 cm height) Ti alloy sample (Ti6Al4V grade 5) placed under a 180 MeV proton pencil beam. A measurement error of approx. 0.5% is expected (Vai *et al* 2019). A detailed description of the measurement of SPR using the MLIC can be found in Fellin *et al* (2017).

To check the pCT system calibration, a measurement of the water's SPR has been carried out using demineralized water. Its SPR distribution has been fitted with a Gaussian function and its mean value compared to the NIST expected value for demineralized water.

2.2. Phantoms and implant devices

In this study we measured the SPR maps of a variety of implant materials and devices with the pCT apparatus described in the previous section. All samples were immersed in a dedicated phantom filled with demineralized water and kept at room temperature (21 °C) during the measurement session.

First, the pCT technique has been applied to a homogeneous cylindrical (3 cm diameter, 1 cm height) Ti alloy sample (Ti6Al4V grade 5). This object is mounted in a foam insert and immersed in demineralized water within a cylindrical delrin container of 15 cm external diameter and wall thickness 15 mm (*phantom* #1).

Then, a set of devices used for prostheses (see figure 2(a) and table 1 for a detailed description) have been inspected by pCT (*phantom* #2). In this case, the phantom uses the same delrin container filled with demineralized water. All devices and materials have been glued to the bottom of the container. A picture of *phantom* #2, placed on the rotating platform between the second and third planes of the pCT tracker, is shown in figure 2(b).

Further, we inspected by pCT an intra-vertebral titanium alloy implant system made of various components. Figures 2(c) and (d) show pictures of the system, consisting of a three-dimensional (3D) meshed cage, support rods, screws and plastic structures mimicking a vertebral body. The system is larger than the FoV of the pCT scanner. In figure 2(c), the yellow rectangle indicates the region within the FoV, inspected in this work. A close-up of the Ti- alloy lattice structure is shown in figure 2(d); the zoomed image reveals the presence of an internal structure. This implant has been placed in a 11 cm diameter cylindrical PET container, about 1.5 mm thick, filled with demineralized water (*phantom* #3).

Finally, the SPR value for water obtained with *phantom* #3 has been compared with the NIST standard reference to cross-check the pCT system calibration.

2.3. Spatial resolution and partial volume effect

Some of the objects whose SPR is measured in this work, have dimensions close to the spatial resolution of the pCT system and could suffer from the partial volume effect. To mitigate this possible measurement bias, the tomographic images used in this work have not been processed with a Hann filter, but for the case of xCT/pCT comparison (see section Discussion). This maximizes the position resolution (Fogazzi *et al* 2023) with the aim of reducing the partial volume effect in small sized devices. In this respect, it is important to have an evaluation of the pCT spatial resolution to consequently define ROIs which are well within the samples, to have realistic measurements of the SPR in these regions.

This was done by fitting abrupt material discontinuities (edges) with 'edge spread functions' (ESF) defined as:

$$f(x) = a + b * \mathrm{Erf}\left((x - c)/d\right) \tag{1}$$

where a,b,c and d are fit parameters and Erf is an 'error function' along radial direction. The derivative of the ESF, i.e. the 'line spread function' (LSF), is then calculated; this is a Gaussian with a standard deviation of $\sigma = d/\surd 2$. The modulus of the Fourier transform of the LSF, the modulation transfer

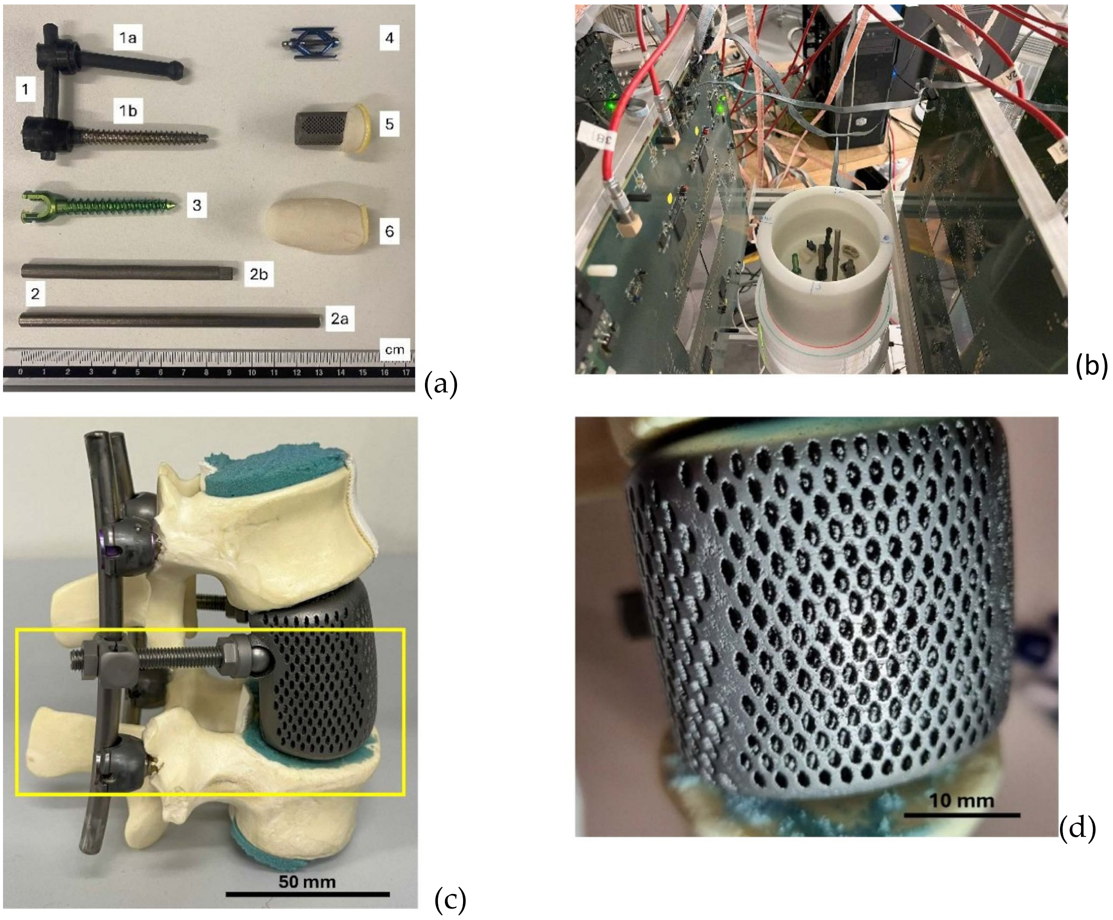

Figure 2. (a) Implant devices inspected by the pCT system: their description is reported in table 1. (b) *Phantom* #2 with the prosthesis' devices installed in the pCT system. (c) Photograph of the intra-vertebral titanium implant used for *phantom* #3; the yellow rectangle indicates the field-of-view of the tomographic image shown in this paper. (d) Detail of the Ti- alloy lattice structure.

Table 1. List of prosthesis' materials of *phantom* #2 inspected by the pCT system.

Device number	Description
1	Carbon rod (1a) with a titanium-coated carbon screw (1b)
2	Titanium rods (6 mm diameter)
3	Titanium screw
4	Titanium vertebral thickness regulator
5	Titanium drilled cage
6	Barium-loaded polymethyl methacrylate (PMMA)

function (MTF), is again a Gaussian, but it is a function of the spatial frequency. The value at which the MTF decays below 10% of its value at zero frequency is (Krah *et al* 2018):

$$R_{0.1}\left[\mathrm{lp\ mm}^{-1}\right] = \frac{\sqrt{2\ln 10}}{2\pi}\frac{1}{\sigma\,[\mathrm{mm}]}. \tag{2}$$

$R_{0.1}\left[\mathrm{lp\ mm}^{-1}\right]$ is used as a 'figure of merit' of the spatial resolution of an imaging system (Richard *et al* 2012). The spatial resolutions obtained with this approach are then compared with those extensively presented in Fogazzi *et al* (2023), to check for consistency.

Three- or two-dimensional ROIs are graphically defined in the tomography volume using the imaging program Fiji (Schindelin *et al* 2012). The same program is then used to extract histograms or profiles of the SPR of the image voxels falling in these ROIs. The ROIs for SPR histograms are chosen in such a way to be well separated from material edges, to minimize partial volume, but large enough to

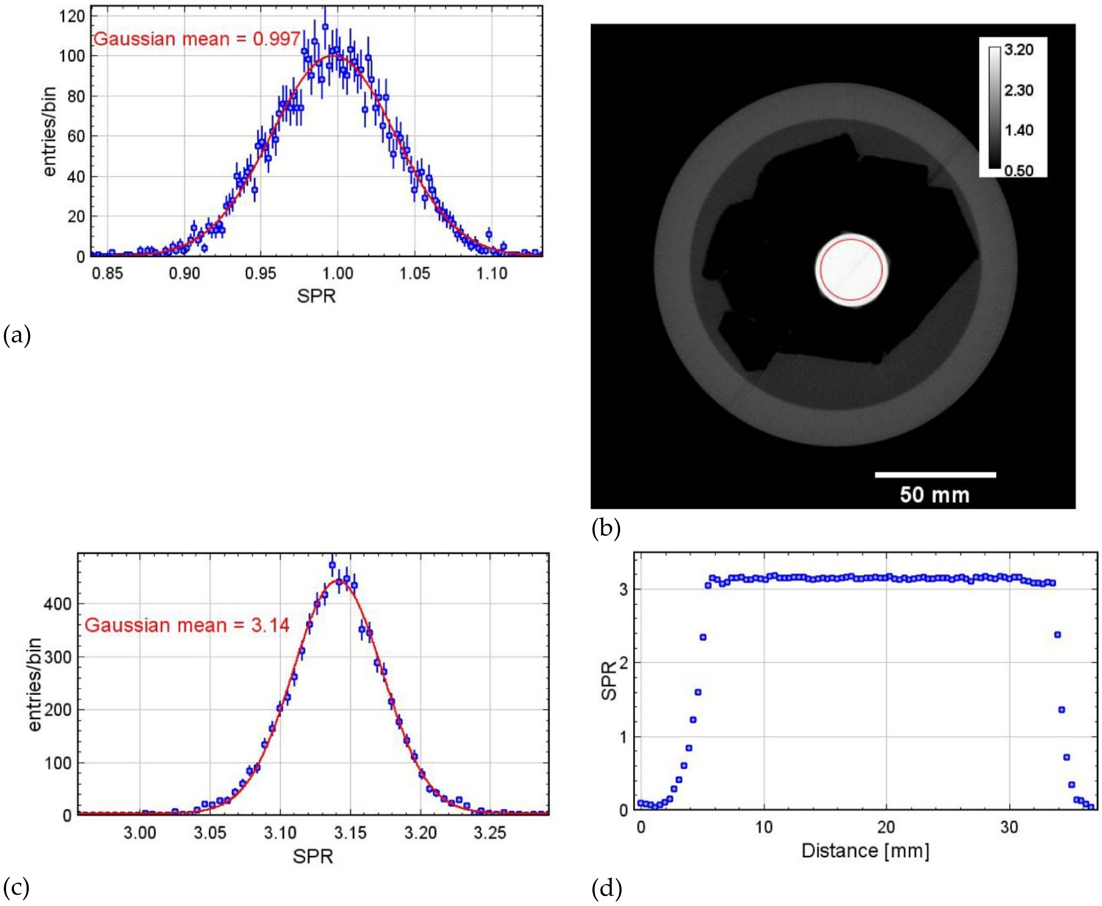

(a)

(b)

(c)

(d)

Figure 3. (a) SPR distribution of the voxels contained in a demineralized water ROI of *phantom* #3 together with a Gaussian fit; (b) axial section (slice #1–4 averaged) of *phantom* #1 with ROI in red. (c) SPR distribution of the voxels contained in the Ti6Al4V alloy ROI together with a Gaussian fit. The Gaussian mean values from both fits are shown in the legend. (d) Profile of the SPR across the Ti6Al4V alloy sample of *phantom* #1; error bars are smaller than symbols.

contain relevant voxel statistics. The ROIs for profiles are large enough to contain edges and homogenous bulk materials.

The SPR histograms obtained after this procedure are fitted with a Gaussian function to extract the mean value.

A separate study on the ROI choice has been done for the particular case of the Polymethylmethacrylates (PMMA) cement sample which has an irregular shape and bubble inclusions.

2.4. xCT/pCT comparison set-up

A direct comparison between xCT and pCT images of phantoms with metallic prostheses has been carried out. The xCT of the intravertebral system has been acquired with a Big Bore Brilliance CT scanner (Philips Medical Systems, Cleveland, OH, USA) at the Trento Proton Therapy Center, 120 kVp and 12-bit acquisition modality, same conditions as described in Fogazzi *et al* (2023) implemented with an O-MAR (Metal Artifact Reduction for Orthopedic Implants) filter and same voxel dimensions as those used in pCT. To compare with the xCT, the pCT image has been reconstructed using a Hann filter with cut-off frequency 0.65 times the Nyquist frequency. In fact, as discussed in Fogazzi *et al* (2023), this configuration meets the condition of same spatial resolution for the two techniques.

3. Experimental results

3.1. SPRs of homogeneous samples

Demineralized water SPR distribution fitted with a Gaussian function is shown in figure 3(a). The Gaussian mean from the fit is 0.997 ± 0.007.

The SPR of the homogeneous Ti6Al4V alloy sample has been measured using *phantom* #1. Figure 3(b) shows an axial section (slice #1–4 averaged) of *phantom* #1. The titanium sample is placed at the centre held in place by a low density foam surrounded by water. The SPR distribution within a

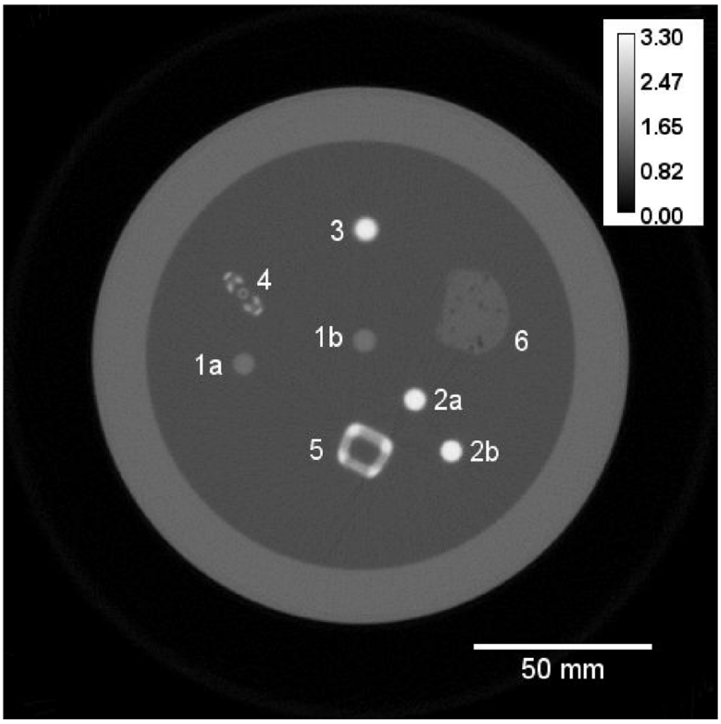

Figure 4. An axial slice of the prosthesis material and device phantom (*phantom* #2). Labels identify the devices described in table 1. Gray scale indicates the SPR values.

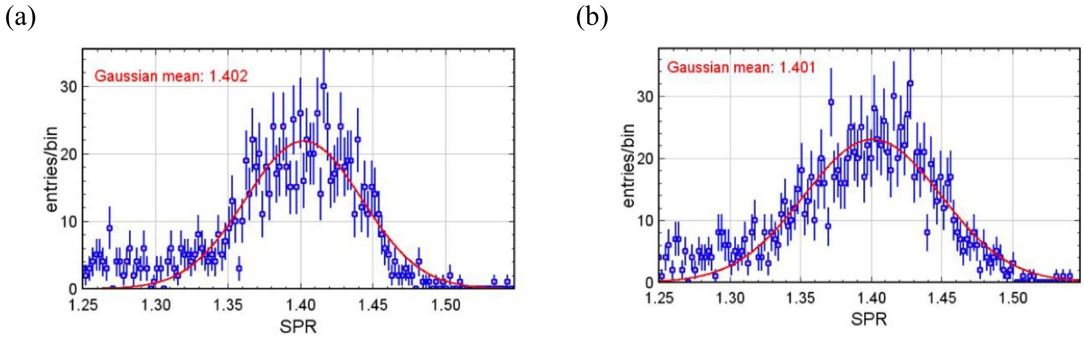

Figure 5. SPR distribution of the voxels inside 3D ROIs of *phantom* #2 identifying (a) the carbon rod #1*a* and (b) carbon screw #1*b*. The curve superimposed is a fit with a Gaussian function.

2.5 cm diameter, 6 mm height cylindrical ROI (evidenced in red) coaxial to the specimen is shown in figure 3(c). The fitted Gaussian mean value of the Ti6Al4V SPR is 3.14 ± 0.02. Figure 3(d) shows a profile of the SPR across the cylindrical Ti alloy sample.

For comparison, the SPR of the Ti6Al4V alloy material has been independently determined placing the same Ti cylinder of *phantom* #1 in front of the MLIC and measuring the shift of the Bragg peak of a 180 MeV proton beam in the calibrated ionization chambers of the instrument with respect to its position without the cylinder. The resulting SPR value is 3.17 ± 0.02.

3.1.1. SPRs of implant materials and devices

Figure 4 shows an axial section of the tomographic reconstruction of *phantom* #2. The prostheses materials and devices are clearly visible and identified with labels as listed in table 1.

Figure 5 shows the SPR distribution of the voxels inside 3D ROIs identifying the carbon devices #1*a* (left) and #1*b* (right). The SPR mean values are 1.402 ± 0.009 and 1.401 ± 0.009 for #1*a* and #1*b* respectively. The two values are in agreement, considering their errors, highlighting that the Titanium coating of the screw #1*b* has no, or little, influence on the SPR measurements on the internal part of the device where the ROI is located.

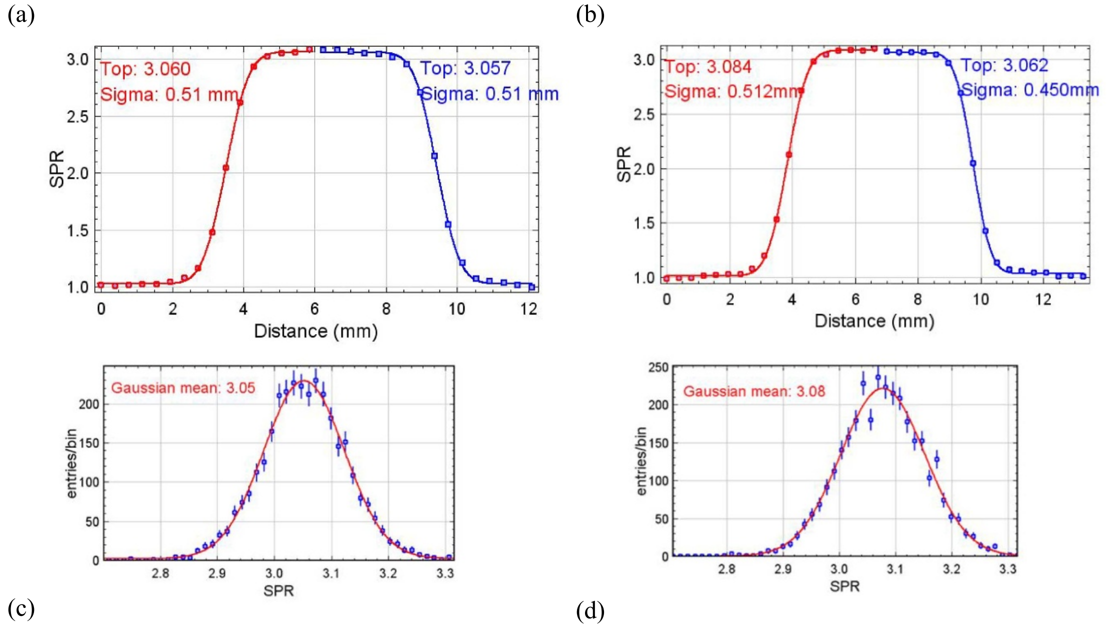

Figure 6. (a–b) SPR profile along the diameters of the #2*a* and #2*b* rods averaged on axial slices n. 2–26; the edges of the distributions are fitted with the ESF as defined in equation (1) of section 2.3. In the legend of (a) and (b) the top value of the fitted functions together with the sigma as defined in equation (1) of section 2.3 are indicated. (c–d) SPR distribution of the voxels inside cylindrical 3D ROIs (2.34 mm diameter, 3.85 mm height) identifying rods #2*a* and #2*b*. Curves superimposed in (c–d) are fits with Gaussian functions whose mean values are indicated in the legend.

Figures 6(a) and (b) show the SPR profiles along the diameter of rods #2*a* and #2*b* in figure 4, with, superimposed, the fit with ESF as defined in equation (1) of section 2.3. The sigma of the fitted ESFs have values of about $0.45-0.5$ mm as reported in figures 6(a) and (b) insets. Using these values, the resolution parameter $R_{0.1}$, as defined in equation (2) of section 2.3, for rod #2*a* and #2*b* is $0.7-0.75\,\mathrm{lp\,mm^{-1}}$ compatible with the measurements reported in Fogazzi *et al* (2023). Using the fit parameters of the ESF the distance from the nominal edge of the profiles where the partial volume effect reduces to less than 5% is about 1 mm leaving a radius of about 4 mm to a ROI which is only barely affected by the partial volume effect. In fact, the flat tops of both profiles 6 (a) and (b) have size about 3.51 mm (9 voxels) so, using cylindrical ROIs with a conservative diameter value of 2.34 mm (6 voxels) and a length of 38.5 mm, the SPR of the titanium-alloy rods elements #2*a* and #2*b* can be correctly evaluated. The SPR distributions for rod #2*a* and #2*b* in these ROIs are shown, respectively, in figures 6(c) and (d) together with a Gaussian fit superimposed. The rod #2*a* has a mean SPR of 3.05 ± 0.02 while rod #2*b* is 3.08 ± 0.02. These two SPR values are compatible, among each other, within the error of the measurement.

Figure 7(a) shows, together with two pictures of the drilled cage #5, a zoom of the axial slice in the region containing it. Figure 7(b) shows the SPR profile along the ROI evidenced in yellow in figure 7(a). The ROI is one axial slice #5, 1.5 mm thick; section is 3 × 59 pixels (1.17×23.01 mm^2). In the regions of solid corners, we measure an SPR value of about 3, similar but slightly lower than that of rods #2*a* and #2*b*. Figure 7(b) evidences a significant partial volume effect in the drilled regions, where an effective SPR value of about 1.8 is measured, due to the contributions of the titanium and the water filling the holes.

Figure 8 shows the coronal view of the Ti self-tapping screw, #3. To enhance the fine details, reconstruction voxel size has been reduced to $0.39 \times 0.39 \times 0.39$ mm^3. In this way, the threads of the 3.0 mm pitch self-tapping screw are clearly resolved. The SPR of the screw's material, measured in a ROI (red rectangle in figure 8) located around the axis of the device, is 3.04 ± 0.02.

We also imaged a jack (#4) used in vertebral surgery, an axial section of this device is visible in figure 4. The dimensions of this object are so small that the partial volume effect dominates and the SPRs are closer to one, the value of the water background, than to that of the titanium material. Nevertheless, the construction details of this tiny device are very clearly depicted in the pCT tomography.

Object #6 is a piece of barium-loaded PMMA cement. Three different ROIs centred in same point have been defined to better evaluate the influence of air inclusion and the irregular shape of the cement

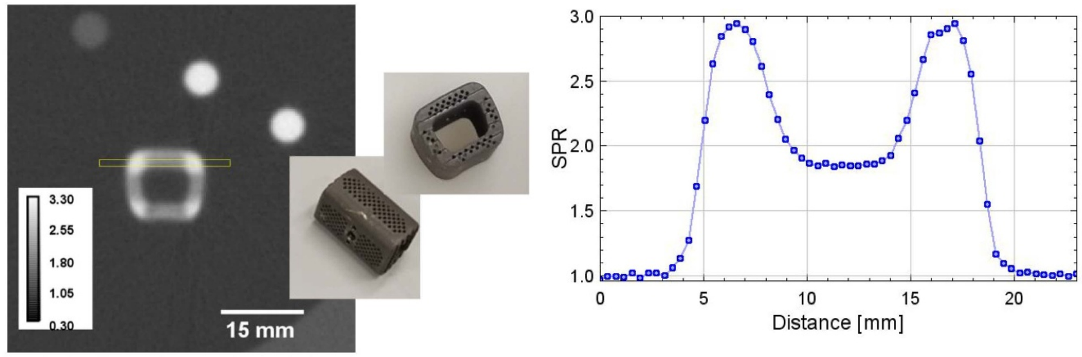

(a) (b)

Figure 7. (a) zoom of axial slice in the correspondence of device #5 pictured in insets. (b) SPR profile along the ROI shown in yellow in (a).

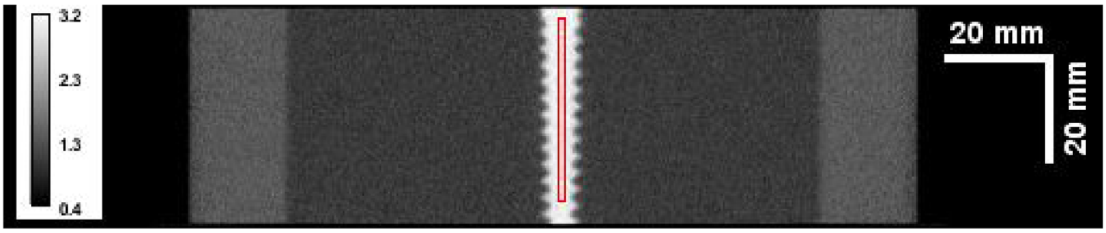

Figure 8. Coronal view of the self-tapping screw #3, showing the 3 mm pitch screw threads. Reconstruction voxel size of this image is 390 μm × 390 μm × 390 μm. The ROI used to measure the material SPR is highlighted in red.

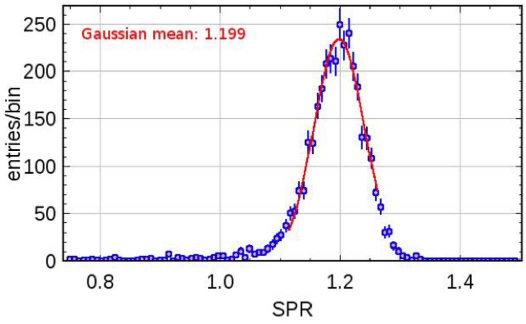

Figure 9. Distribution of the SPR in ROI2 (see text) within the cement material; the distribution is fitted using a Gaussian in a region of SPR between 1.1 and 1.3.

sample. One (ROI1) has 20 × 30 × 18 (x,y,z) voxels, a second one (ROI2) is smaller 10 × 20 × 15 (x,y,z) voxels and a last one (ROI3) is located in the core of the cement piece: 6 × 16× 15 (x,y,z) voxels. The average value of the SPR in these regions is 1.198 with a standard deviation of 0.003. Taking this into account, the total error on SPR for this measurement is 0.009. Figure 9 shows the SPR distribution of this material in case of ROI2.

To summarize, the pCT measurements of the SPR of all inspected materials are listed in table 2. Apart from demineralized water and Ti alloy Ti6Al4V, the composition of the listed items is unknown, so the measurement could not be compared to reference values.

3.2. Intra-vertebral titanium alloy implant system

Figures 10(a) and (b) show two axial sections of the tomographic reconstructions of the intravertebral Ti alloy structure studied in this work (*phantom* #3, see figures 2(c) and (d)). Beyond the internal grid (figure 10(a)), other details of the intra-vertebral prosthesis which are resolved by the pCT image are the head of the two self-tapping screws which fix the titanium cage to the vertebral bodies (figure 10(d)). Due to the inclined direction of the screws with respect to the tomography axial plane, only the initial

Table 2. Summary of SPR measurements using the pCT system for different prosthesis materials.

	pCT measurement	Reference
Demineralized water	0.997 ± 0.007	**0.998**[a]
Titanium alloy (Ti6Al4V)	3.14 ± 0.02	3.17 ± 0.02 [b]
Rod (#2*a*)	3.05 ± 0.02	—
Rod (#2*b*)	3.08 ± 0.02	—
Screw (#3)	**3.04**± 0.02	—
Carbon rod (#1*a*)	1.402 ± 0.009	—
Carbon screw (#1*b*)	1.401 ± 0.009	—
Bone Cement (PMMA + Ba)	1.198 ± 0.009	—

[a] NIST value for water at 21 °C.

[b] value measured with MLIC.

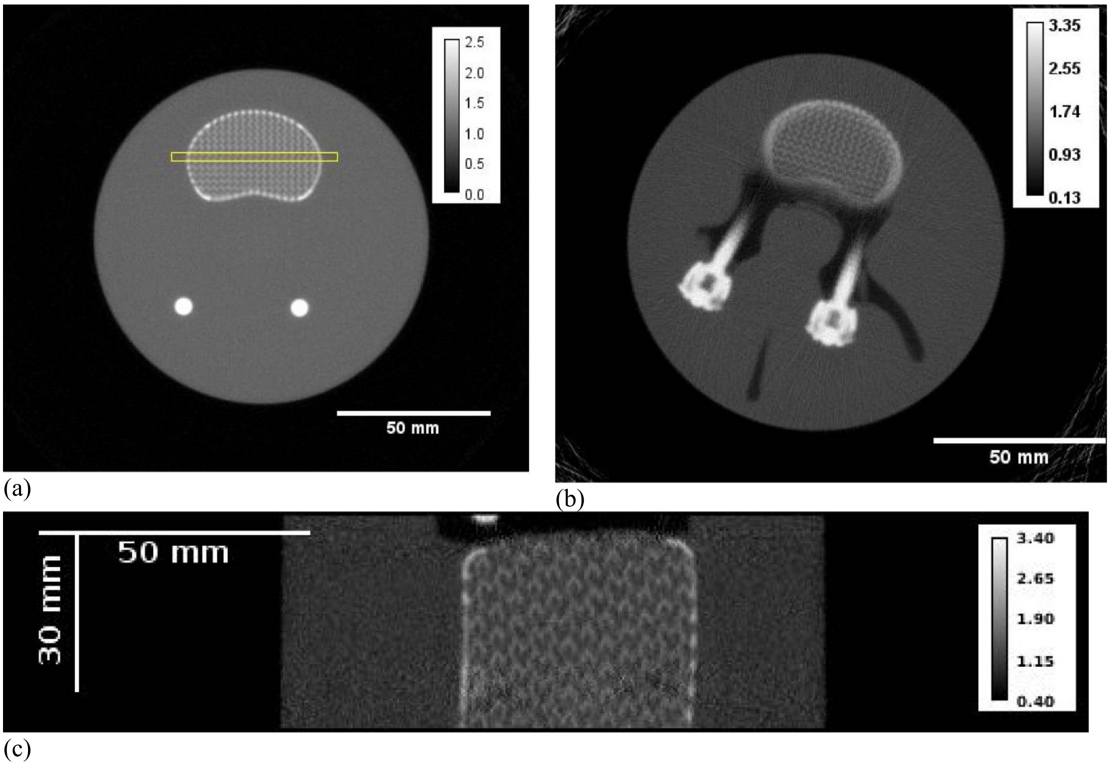

Figure 10. (a)–(b) tomographic reconstructions of axial sections of the intravertebral Ti alloy structure; (c) coronal section of the 3D vertebral Ti cage showing its internal structure.

part of each screw is visible. A coronal section of the 3D cage, with details of its internal structure, is shown in figure 10(c).

An SPR profile following the yellow box in figure 10(a) along the 3D mesh structure in the intravertebral cage, is shown in figure 11. The spatial resolution of our system, being about 0.7 lp mm^{-1}, allows us to resolve the 2.3 mm grid pitch, but the SPR mean value is underestimated due to the partial volume effect. This, once again, evidences the fact that devices need to be sufficiently large for a correct SPR determination.

Finally, a direct comparison between xCT and pCT images of phantoms with metallic prostheses has been carried out, using the set-up described in section 2.4. In figures 12(a) and (b) we show respectively the xCT/pCT images of an axial slice of *phantom* #3, in full HU/SPR scale range. Both images have been reconstructured using $0.39 \times 0.39 \times 1.5$ mm^3 voxel size. The cut in the upper part of xCT image is due to incomplete filling of water in the container, having placed *phantom* #3 horizontally on the xCT couch. We selected one ROI 25 mm long and 1.56 mm wide on both images (in yellow), in same position, in view to intercept one Ti-alloy bar. Corresponding profile plots are shown respectively in figure 12(c) and (d).

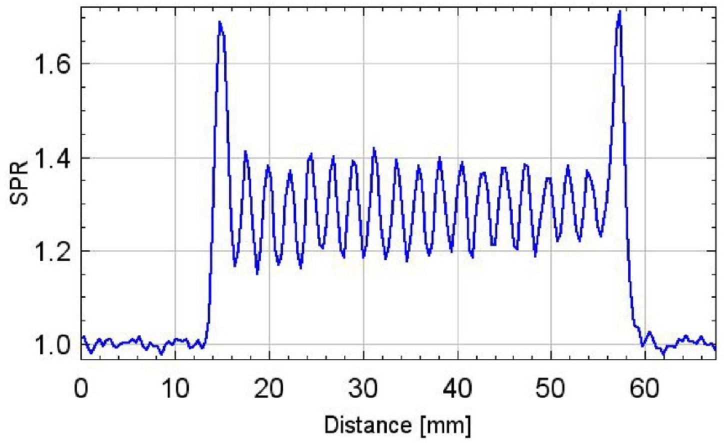

Figure 11. SPR profile along the yellow box in figure 10(a) of the 3D mesh structure in the intraventebral cage.

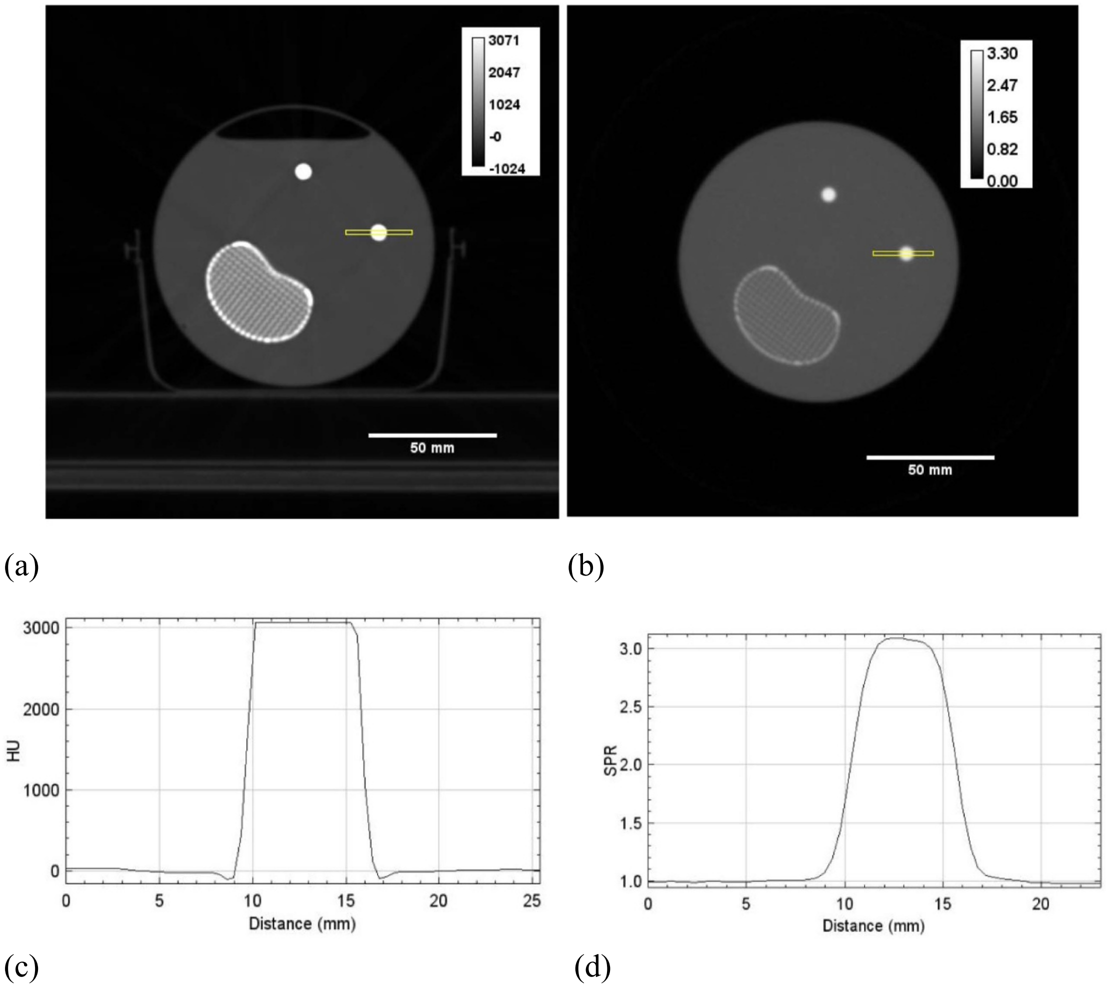

Figure 12. (a) xCT and (b) pCT image of the intravertebral system with full HU/SPR scale. Selected ROIs are shown in yellow. Full scale ROI profile plots for (c) xCT and (d) pCT .

4. Discussion

The two images in figure 12 (a) and (b) evidence a similar spatial resolution for xCT and pCT, and a better contrast for xCT, as expected. Nonetheless, figure 12(c) shows that the Ti-bar profile in case of the xCT appears to be saturated at 3071HU, the highest value of the 12-bit xCT scanner. On the contrary, the Ti bar profile in case of the pCT image shown in figure 12(d) is clearly not saturated. Its

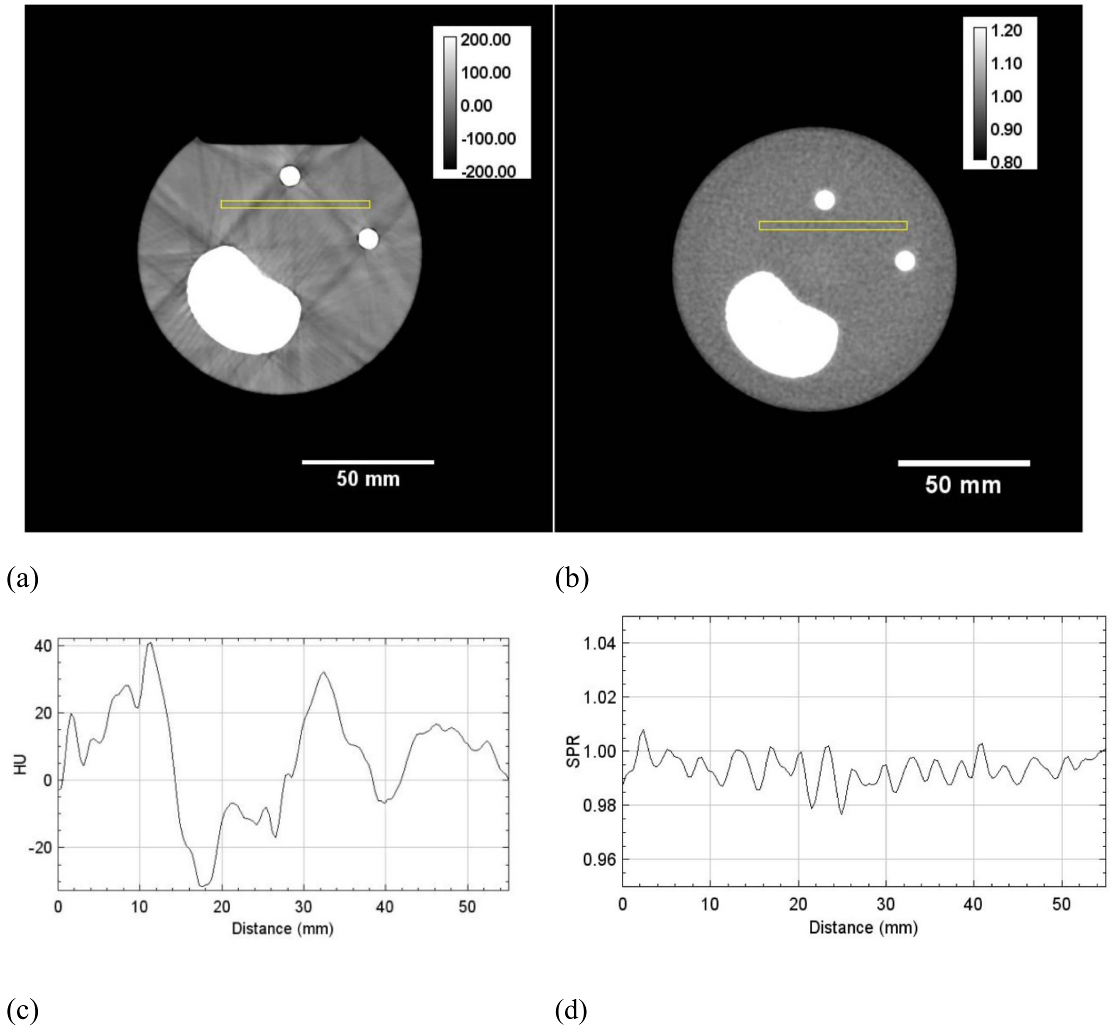

(a) (b)

(c) (d)

Figure 13. (a) xCT and (b) pCT images of the intravertebral system with enhanced HU/SPR scale ± 20% of water value. Selected ROIs are shown in yellow. ROI profile plot for (c) xCT and (d) pCT, SPR scale is ± 5% for both.

average value is 3.07 ± 0.02, in a ROI with a 2.34 mm diameter, compatible with what measured for e.g. rods #2(a,b) and screw #3 (see table 1). The saturation issue could be in principle resolved using a 16-bit xCT (Glide-Hurst *et al* 2013). Nonetheless, to determine a calibration curve HU/SPR with xCT in this extended range and pCT for non-biological materials, we would need a set of measurements on certified materials with known composition. This study will be the subject of a forthcoming work.

To evidence the presence of artifacts, in figure 13(a) and (b) we show respectively the xCT/pCT images of the same phantom in a scale range ± 20% of the HU/SPR water values. We selected one ROI 55 mm long and 3 mm wide on both images (in yellow) in same position within the water region, to analyze the presence of artifacts. Corresponding profile plots are shown in figure 13(c) and (d), where the scale is ± 5% of the water value. The xCT image (figure 13(a)) evidences the presence of artifacts which are negligible in the pCT one (figure 13(b)). This is reflected in the ROI profiles which are, for pCT, within ±1%, whereas for xCT about ±4%.

Results and discussion presented above evidence that artifacts in images and fluctuations in profiles of metal objects made with conventional x-CT can be significantly reduced when using pCT.

Even more significantly, pCT shows to be able to measure the SPR of metal objects where xCT saturates to the maximum HU value. A conventional xCT would not be able to distinguish e.g. the homogeneous Ti6Al4V alloy sample from rods #2*a* and #2*b* and screw #3 for what concerns SPR values. Additionally, cement, being radiopaque, would appear saturated on an xCT image, as if it were a metal, despite its SPR, measured by pCT as 1.198 ± 0.009 (see table 1). These results demonstrate the superior ability of pCT in directly evaluating SPRs in case of materials and devices currently used for prostheses. SPR values so determined for a variety of materials and devices, can be used to create an effective average SPR map, to be used as a voxel-by-voxel substitute in those regions of xCT-derived images affected by saturations. This could be of help both during the contouring phase of target volumes and organs at risk as well as to improve the dose calculation accuracy of TP activities in particle therapy.

5. Conclusions

This study presents the first application of the pCT methodology to directly measure SPR maps of complex metallic prostheses. To this end, different materials and devices used for surgical implantation of the prostheses were investigated using a prototype pCT system under a proton beam of therapeutic energies. Since our measurements have been performed at 21 °C, the expected demineralized water SPR is 0.998. Indeed, the pCT SPR measured for water is 0.997 ± 0.007, in very good agreement with what is expected, confirming the validity of the experimental method. Moreover, a homogeneous Ti6Al4V alloy sample has been inspected by pCT. The SPR measured (3.14 ± 0.02) for this material compares well to what was obtained with the same sample by an independent method using an MLIC (3.17 ± 0.02).

A set of devices and materials used for prostheses, with variable geometries and unknown compositions, have been inspected by pCT and their SPRs have been determined. Results are consistent with SPRs characteristics of carbon and Ti alloys for rods and screws and with PMMA in case of cement.

The fine spatial resolution of our system, i.e. about 0.7 lp mm^{-1}, allowed us to resolve details within a millimeter scale. In the case of inhomogeneous and tiny structures, the effect of pCT spatial resolution has been studied with the aim of determining proper ROIs wherein SPRs are not affected by partial volume effects. In the case of smaller structures, where the partial volume effect cannot be avoided, values measured by pCT have been considered as averages of the materials involved, namely as effective SPRs.

Finally, a complex intra-vertebral titanium alloy implant system, made of a 3D meshed cage, support rods, screws and plastic structures simulating vertebrae has been inspected by pCT. The reconstructed images allowed us to reveal fine details of the internal 3D meshed grid structure of the metal cage as well as of the screws connecting it to the vertebrae.

In conclusion, pCT ability to correctly determine mean values of the SPRs of metallic devices has been proved experimentally. Moreover, the ability of this technique in reconstructing complex metal structures within the millimetric size with negligible artifacts has been demonstrated.

Given the promising results of this study, future work will focus on extending the SPR characterization of other materials of clinical interest and on applying SPR effective values so determined in particle therapy TP activities. Moreover, a calibration curve HU/SPR with xCT in the 16-bit extended range and pCT for non-biological materials is planned and will be the subject of a forthcoming work.

Data availability statement

The data cannot be made publicly available upon publication because they are not available in a format that is sufficiently accessible or reusable by other researchers. The data that support the findings of this study are available upon reasonable request from the authors.

Acknowledgments

This work has been performed in the framework of the pRAD experiment funded by Istituto Nazionale di Fisica Nucleare—Commissione Scientifica Nazionale 5, Istituto Nazionale di Fisica Nucleare (INFN-CSN5).

ORCID iDs

Mara Bruzzi 0000-0001-7344-8365
Monica Scaringella 0000-0002-6753-2832
Elena Fogazzi 0000-0002-2527-4070
Francesco Tommasino 0000-0002-8684-9261
Enrico Verroi 0000-0003-0957-4505
Carlo Civinini 0000-0002-4952-3799

References

Abd-Elaziem W, Darwish M A, Hamada A and Daoush W M 2024 Titanium-Based alloys and composites for orthopedic implants applications: a comprehensive review *Mater. Des.* **241** 112850

Andersson K M, Dahlgren C V, Reizenstein J, Cao Y, Ahnesjö A and Thunberg P 2018 Evaluation of two commercial CT metal artifact reduction algorithms for use in proton radiotherapy treatment planning in the head and neck area *Med. Phys.* **25** 4329–44

Bashkirov V A, Johnson R P, Sadrozinski H F-W and Schulte R W 2016 Development of proton computed tomography detectors for applications in hadron therapy *Nucl. Instrum. Methods Phys. Res. A* **809** 120–9

Berger M J, Coursey J S, Zucker M A and Chang J 2017 (NIST Standard Reference Database 124) Stopping-power&range tables for electrons, protons, and helium ions (https://doi.org/10.18434/T4NC7P)

Branco D, Kry S, Taylor P, Zhang X, Rong J, Frank S and Followill D 2021 Dosimetric impact of commercial CT metal artifact reduction algorithms and a novel in-house algorithm for proton therapy of head and neck cancer *Med. Phys.* **48** 445–55

Bruzzi M *et al* 2017 Proton computed tomography images with algebraic reconstruction *Nucl. Instrum. Methods Phys. Res. A* **845** 652–5

Chhabra M A *et al* 2024 Proton therapy for spinal tumors: aconsensus statement from the particle therapy cooperative group *Int. J. Radiat. Oncol. Biol. Phys.* **120** 1135–48

Civinini C, Scaringella M, Brianzi M, Intravaia M, Randazzo N, Sipala V, Rovituso M, Tommasino F, Schwarz M and Bruzzi M 2020 Relative stopping power measurements and prosthesis artifacts reduction in proton CT *Phys. Med. Biol.* **65** 225012

Cofano F *et al* 2020 Carbon fiber reinforced vs titanium implants for fixation in spinal metastases: a comparative clinical study about safety and effectiveness of the new "carbon-strategy *J. Clin. Neurosci.* **75** 106–11

Feldkamp I A, Davis L C and Kress J W 1984 Practical cone beam algorithm *J. Opt. Soc. Am. A* **1** 612–9

Fellin F, Righetto R, Fava G, Trevisan D, Amelio D and Farace P 2017 Water equivalent thickness of immobilization devices in proton therapy planning–modelling at treatment planning and validation by measurements with a multi-layer ionization chamber *Phys. Med.* **35** 31–38

Fogazzi E, Trevisan D, Farace P, Righetto R, Rit S, Scaringella M, Bruzzi M, Tommasino F and Civinini C 2023 Characterization of the INFN proton CT scanner for cross-calibration of x-ray CT 2023 *Phys. Med. Biol.* **68** 124001

Glide-Hurst C, Chen D, Zhong H and Chetty I J 2013 Changes realized from extended bit-depth and metal artifact reduction in CT *Med. Phys.* **40**

Jakel O and Reiss P 2007 The influence of metal artefacts on the range of ion beams *Phys. Med. Biol.* **52** 635–44

Jia Y C Y, Zhao L, Cheng C W, McDonald M W and Das I J 2015 Dose perturbation effect of metallic spinal implants in proton beam therapy *J. Appl. Clin. Med. Phys.* **16** 333–43

Johnson R P 2024 Meeting the detector challenges for pre-clinical proton and ion computed tomography *Phys. Med. Biol.* **69** 11TR02

Knopf A C and Lomax A 2013 *In vivo* proton range verification: a review *Phys. Med. Biol.* **58** 131–60

Krah N, Khellaf F, Létang J M, Rit S and Rinaldi I 2018 A comprehensive theoretical comparison of proton imaging set-ups in terms of spatial resolution *Phys. Med. Biol.* **63** 135013

Le Fèvre C, Lacornerie T, Noël G and Antoni D 2022 Clinical practice guidelines : management of metallic implants in radiotherapy Gestion des implants métalliques en radiothérapie *Cancer/Radiothérapie* **26** 411–6

Long Maziyar J R, Kalani A, Goulding K A, Ashman J B and Flug A J 2023 Carbon-fiber-reinforced polyetheretherketone orthopedic implants in musculoskeletal and spinal tumors: imaging and clinical features *Skelet. Radiol.* **52** 393–404

Mairani A, Böhlen T T, Schiavi A, Tessonnier T, Molinelli S, Brons S, Battistoni G, Parodi K and Patera V 2013 A Monte Carlo-based treatment planning tool for proton therapy *Phys. Med. Biol.* **58** 2471

Moteabbed M, Bobić M, Paganetti H and Efstathiou J A 2024 The role of proton therapy for prostate cancer in the setting of hip prosthesis *Cancers* **16** 330

Njiti M M, Osman N D, Mansor M S, Rabaiee N A and Abdul Aziz M Z 2024 Potential of metal artifact reduction (MAR) and deep learning-based reconstruction (DLR) algorithms integration in CT metal artifact correction: a review *Radiat. Phys. Chem.* **218** 111541

Oancea C, Ambrožová I, Popescu A I, Mytsin G, Vondráček V and Davídková M 2018 LET spectra behind high-density titanium and stainless steel hip implantsirradiated with a therapeutic proton beam *Radiat. Meas.* **110** 7–13

Poel R, Bel)osi F, Albertini F, Walser M, Gisep A, Lomax A J and Weber D C 2020 Assessing the advantages of CFR-PEEK over titanium spinal stabilization implants in proton therapy—a phantom study *Phys. Med. Biol.* **65** 245031

Richard S, Husarik D B, Yadava G, Murphy S N and Samei E 2012 Towards task-based assessment of CT performance: system and object MTF across different reconstruction algorithms *Med. Phys.* **39** 4115–22

Rit S, Dedes G, Freud N, Sarrut D and Létang J M 2013 Filtered backprojection proton CT reconstruction along most likely paths *Med. Phys.* **40** 031103

Rousselle A, Amelot A, Thariat J, Jacob J, Mercy G, De Marzi L and Feuvret L 2020 Metallic implants and CT artefacts in the CTV area: where are we in2020? *Cancer/Radiothérapie* **24** 658–66

Sadrozinski H F-W *et al* 2003 Issues in proton computed tomography *Nucl. Instrum. Methods Phys. Res. A* **511** 275–81

Scaringella M, Bruzzi M, Farace P, Fogazzi E, Righetto R, Rit S, Tommasino F, Verroi E and Civinini C 2023 The INFN proton computed tomography system for relative stopping power measurements: calibration and verification *Phys. Med. Biol.* **68** 154001

Schindelin J *et al* 2012 Fiji: an open-source platform for biological-image analysis *Nat. Methods* **9** 676–82

Schneider U, Pedroni E and Lomax A 1996 The calibration of CT Hounsfield units for radiotherapy treatment planning *Phys. Med. Biol.* **41** 111–24

Schulte R W, Penfold P S, Tafas J T and Schubert K E 2008 A maximum likelihood proton path formalism for application in proton *Med. Phys.* **35** 4849–56

Selles M, van Osch J A C, Maas M, Boomsma M F and Wellenberg R H H 2024 Advances in metal artifact reduction in CT images: a review of traditional and novel metal artifact reduction techniques *Eur. J. Radiol.* **170** 111276

Snider J W *et al* 2018 Long-term outcomes and prognostic factors after pencil-beam scanning proton radiation therapy for spinal chordomas: a large, single-institution cohort *Int. J. Radiat. Oncol. Biol. Phys.* **101** 226–33

Tommasino F *et al* 2017 Proton beam characterization in the experimental room of the trento proton therapy facility *Nucl. Instrum. Methods Phys. Res. A* **869** 15–20

Vai A *et al* 2019 Characterization of a MLIC detector for QA in scanned proton and carbon ion beams *Int. J. Part. Ther.* **6** 50–59

Williams D C 2004 The most likely path of an energetic charged particle through a uniform medium *Phys. Med. Biol.* **49** 2899–911